Contents lists available at ScienceDirect

Nano Energy

journal homepage: http://ees.elsevier.com

High-energy all-in-one stretchable micro-supercapacitor arrays based on 3D laser-induced graphene foams decorated with mesoporous ZnP nanosheets for self-powered stretchable systems

Cheng Zhang [a,c,*], Zhixiang Peng [a], Chunlei Huang [a], Bingwen Zhang [a], Chao Xing [a], Huamin Chen [a], Huanyu Cheng [b,**], Jun Wang [a,**], Shaolong Tang [c]

[a] Fujian Provincial Key Laboratory of Functional Marine Sensing Materials, College of Physics and Electronic Information Engineering, Minjiang University, Fuzhou 350108, PR China
[b] Department of Engineering Science and Mechanics, Materials Research Institute, Pennsylvania State University, University Park, PA 16802, USA
[c] National Laboratory of Solid State Microstructures, Nanjing University, Nanjing 210093, PR China

ARTICLE INFO

Keywords
Micro-supercapacitor arrays
3D laser-induced graphene foams
Mesoporous non-layered ZnP nanosheets
Improved ionic/electrical conductivities
Stretchable device architecture

ABSTRACT

Micro-supercapacitors are promising energy storage devices that can complement or even replace lithium-ion batteries in wearable and stretchable microelectronics. However, they often possess a relatively low energy density and limited mechanical stretchability. Here, we report an all-in-one planar micro-supercapacitor arrays (MSCAs) based on hybrid electrodes with ultrathin ZnP nanosheets anchored on 3D laser-induced graphene foams (ZnP@LIG) arranged in island-bridge device architecture. The hybrid electrodes with a large specific surface area demonstrate excellent ionic and electrical conductivities, impressive gravimetric (areal) capacitance of 1425 F g^{-1} (7.125 F cm^{-2}) at 1 A g^{-1}, and long-term stability. In addition to high energy (245 m Wh cm^{-2}) and power (12.50 mW kg^{-1} at 145 m Wh cm^{-2}) densities, the MSCAs with excellent cycling stability also showcase adjustable voltage and current outputs through serial and parallel connections of MSC cells in the island-bridge design, which also allows the system to be reversibly stretched up to 100%. Meanwhile, theoretical calculations validated by UV–vis absorption spectra partially suggest that the enhanced capacitance and rate capability may result from the improved electrical conductivity and number of adsorbed charged ions (Na^+ in Na_2SO_4 aqueous electrolyte and K^+ in PVA/KCl gel electrolyte) on the pseudocapacitive non-layered ultrathin ZnP nanosheets. The integration of the all-in-one stretchable MSCAs with a crumpled Au-based triboelectric nanogenerator and stretchable crumpled graphene-based strain sensor demonstrates a self-powered stretchable system. The coupled design principle of electronic materials and device architecture provides a promising method to develop high-performance wearable/stretchable energy storage devices and self-powered stretchable systems for future bio-integrated electronics.

1. Introduction

The portable, wearable, stretchable, and implantable electronic devices are starting to gain momentum in bio-integrated systems for diagnostic confirmation and advanced therapeutic options in clinical medicine [1,2]. These emerging electronics have spurred the rapid development of flexible and stretchable energy harvesting/storage devices with high energy density, superior mechanical stability, and long cycle life [3]. Triboelectric nanogenerators (TENGs) have been proven to be an emerging technology to convert mechanical movement to electrical energy by applying the triboelectric effect [4,5]. The as-produced electricity is generally stored in electrochemical storage devices such as batteries or supercapacitors for driving various wearable electronics [6–8]. Micro-supercapacitors (MSCs) have attracted extensive attention because of their small footprint, high power density, fast charge-discharge, exceptional cycling stability, and facile integration into miniaturized microelectromechanical systems. However, their practical applications still require increased mechanical stretchability and energy density without sacrificing their power density and lifetime [9]. Although various MSCs based on carbon materials or heterostructures have been fabricated using various fabrication approaches [10–13], these devices often suffer from low energy density associated with the electrostatic charge at the electrode-electrolyte interface and limited stretchability due to the presence of non-stretchable active elements and weak inter-

* Corresponding author at: Fujian Provincial Key Laboratory of Functional Marine Sensing Materials, College of Physics and Electronic Information Engineering, Minjiang University, Fuzhou 350108, PR China.
** Corresponding authors.
E-mail addresses: zhangcheng@mju.edu.cn (C. Zhang); huanyu.cheng@psu.edu (H. Cheng); wjnaf@163.com (J. Wang)

https://doi.org/10.1016/j.nanoen.2020.105609
Received 6 August 2020; Received in revised form 5 November 2020; Accepted 11 November 2020
Available online xxx
2211-2855/

face under repeated tensile deformations. Furthermore, the conventional MSCs with sandwich-like stacked geometry in large thickness exhibit poor flexibility, long ion diffusion distances, and complex integration process, thereby presenting significant challenges to integrate with the portable and wearable electronics [14].

Efforts to address the above challenge have led to the exploration of a new class of graphene-like layered pseudocapacitive electrode materials, including MXenes, transition metal dichalcogenides (TMDCs), and layered double hydroxides (LDHs). These electrode materials can provide high redox potential, abundant electrochemical active sites, fast ion diffusion channels, and high mechanical strength to improve supercapacitor performance parameters [15]. It is also well known that all of these 2D materials with layered structures could be easily synthesized by mechanical exfoliation, liquid-phase exfoliation, or selective etching. Nevertheless, 2D materials with layered structures are often associated with a major challenge of inevitable aggregation between layers due to their strong van der Waals interactions [16]. A possible solution to the above issue is to explore the atomically thin non-layered pseudocapacitive electrode materials. As a novel class of 2D materials that enrich the 2D materials family, the non-layered 2D materials can potentially provide higher energy density by tuning their intrinsic properties, such as band-gap, conductivity, and/or defects (e.g., pores, cavities, and dopants) [17]. Driven by this concept, transition-metal phosphides (TMPs, e.g., Co_2P, FeP, Ni_5P_4, MoP, and Cu_3P) have recently been fabricated and demonstrated to exhibit large surface-to-volume ratio, superior electrical conductivity, and a large number of active sites and prominent edges, all of which can contribute to the high energy density [18].

As an advanced stretchable structure, the island-bridge design has been widely explored for stretchable electronics and even planar micro-supercapacitor arrays (MSCAs) with an interdigitated electrode configuration. Compared to the wavy or wrinkled design through a pre-strain/release process, the islands-bridge design can confine strains/deformations to the stretchable interconnects (i.e., "bridges") and significantly reduce the deformation in the active planar MSC cells (i.e., "islands"). This result enables the MSCAs with the island-bridge design to have a higher mechanical stretchable property, while maintaining the electrochemical performance in planar MSC cells. Furthermore, the stretchable interconnects can also allow for serial/parallel connections in the planar MSC cells to result in well-controlled output potentials/currents from the MSCAs. Additionally, the co-planar interdigitated electrodes with a small spacing between fingers reduce the ionic diffusion pathway to produce a high rate capability and power density, along with a decreased thickness for improved flexibility [19]. However, the narrow and long metallic serpentine interconnects dramatically increase the overall resistance and the portion of non-active components to compromise the energy density.

Herein, we report a self-powered stretchable system consisting of all-in-one MSCAs, a crumpled Au-based TENG, and a crumpled graphene-based strain sensor. The all-in-one MSCAs are based on non-layered ZnP ultrathin nanosheets anchored on the three-dimensional (3D) laser-induced graphene foams (LIG), which is configured in the islands-bridge layout. Because of the synergic combination of capacitive and faradaic energy storage materials (mechanisms), the resulting hybrid electrode with drastically minimized inactive material shows excellent electrical conductivity and large ion-accessible surface area. As a result, the all-in-one MSCAs can exhibit high areal (gravimetric) energy density without compromising cycling stability and rate capability. In addition to their excellent electrochemical performance under mechanical bending tests, the all-in-one stretchable MSCAs showcase a negligibly small reduction in their capacitance retention (e.g., a decrease of 2.5% and 2.8% in serial and parallel mode upon a tensile strain of 100%). Moreover, theoretical calculations validated by UV–vis absorption spectra indicate that the ultrathin non-layered ZnP nanosheets have smaller band-gap and larger electrolyte ions adsorption energies than those of ZnO nanosheets. This comparison demonstrates that phosphorization treatment can effectively improve both electronic conductivity and the number of adsorbed charged ions at the electron surface during the charging process. Taken together all of these considerations, the rational design of electrode materials and device architecture has been demonstrated to result in stretchable micro-power sources with high energy density, as well as remarkably improved rate capability and specific capacity. Furthermore, a sensitive and stretchable crumpled graphene-based strain sensor driven by the as-prepared all-in-one stretchable MSCAs showcases the feasibility of a self-powered, well-integrated stretchable system.

2. Experimental section

2.1. Fabrication of samples

2.1.1. Fabrication of electrode materials and all-in-one stretchable MSCAs

The ultrathin ZnP nanosheets were synthesized through fast-heating a homogeneous solution containing $Zn(acac)_3$, CTAB, ethylene glycol, and distilled water, followed by an in situ phosphorization process. First, 1200 mg $Zn(acac)_3$ and 4.4 g CTAB were dissolved into 120 mL ethylene glycol and 22 mL distilled water to form a homogeneous aqueous dispersion. After ultrasonication of 15 min at room temperature, the mixed solution was transferred into a 200 mL Teflon-lined autoclave and heated at 180 °C for 24 h. A drying treatment of the washing product in vacuum overnight yields the ultrathin ZnO nanosheets. Next, 30 mg as-prepared ultrathin ZnO nanosheets and 2 g NaH_2PO_2 were transferred to two porcelain boats in a tube furnace, with NaH_2PO_2 at the upstream side of the furnace. After heating at 300 °C for 2 h in a flowing Ar atmosphere with a heating rate of 3 °C/min, the samples were washed with deionized water and dried in air at 60 °C for 12 h, resulting in the ultrathin ZnP nanosheets.

The stretchable MSCAs were fabricated through a laser irradiation technique followed by a spray coating process using a shadow mask. First, cleaned PI sheets (Cat. No. 2271K3, thickness of 0.01 in.) supported by the PDMS substrate were irradiated by a CO_2 laser cutter system with a pulse duration of ~15 μs to prepare the LIG foam with interdigitated electrodes. Next, the as-synthesized ZnP ultrathin nanosheets were dispersed in a mixture of deionized water, ethanol, and Nafion (5%) (v/v/v ≈ 3:1:0.05) to form a 2 mg mL^{-1} spray ink. The ink was then spray coated on the 3D LIG foam through a shadow mask, followed by the freeze-drying process. Finally, the stretchable MSCAs were obtained after leading wire connection and packaging with a thin PDMS layer with a thickness of 200 μm.

The polymeric gel electrolyte (PVA/KCl) was prepared as follows: 6.5 g of KCl was added into 100 mL deionized water, then 12 g of poly(vinyl alcohol) (PVA) powder was added and magnetically stirred for 4 h in a nitrogen atmosphere using a Schlenk line. The solution was removed at 90 °C for 30 min. Then, the solid electrolyte was drop-coated onto the top surface between the electrodes using a syringe, with a thickness of about 10 μm.

2.1.2. Preparation of resistive strain sensors

The resistive strain sensors based on crumpled graphene film were fabricated through a pre-strain strategy. First, a thin PDMS film was prepared on the graphene grown on a copper substrate by the spin coating method. After completely dissolving the copper substrate in a $FeCl_3$ solution (1 M), the graphene/PDMS composite film was transferred to a uniaxially pre-stretched very-high-bond (3 M VHB 4905) film. Next, peeling the PDMS film left the graphene on the VHB film. After releasing the pre-strain, the crumpled graphene film formed on the VHB film. Finally, the resistive strain sensors based on crumpled graphene film were obtained after leading wire connection and packaging by a thin VHB layer with a thickness of 200 μm.

2.1.3. Preparation of the crumpled Au-based triboelectric nanogenerator (TENG)

To fabricate the crumpled Au-based TENG, PDMS/crumpled Au was used as the triboelectric layer with the other PDMS/Au composite as the collecting electrode. The crumpled-Au film was first prepared through a pre-strain strategy. A PDMS thin film with a thickness of 500 μm was first sputter-coated with a thin layer of gold film using Vacuum Sputter Coater (DP650, France) for 100 s. Next, the PDMS/Au film was transferred to a uniaxially pre-stretched very-high-bond (3 M VHB 4905). After peeling off the PDMS film, the Au film was left on the VHB. Next, the pre-strain in the VHB was lowly relaxed and the crumpled structure of Au film was obtained and then supported by a PDMS substrate. After that, the as-prepared PDMS/crumpled Au (1.5 cm × 1.0 cm) was connected to the other PDMS/Au composite (1.5 cm × 1.0 cm) on top to complete the fabrication of the crumpled Au-based TENG.

2.2. Characterization

The morphology, architecture, electronic properties of as-prepared samples were characterized by an optical camera (D750, Nikon, Japan), scanning electron microscopy (SEM, Hi-tachiS3400), transmission electron microscopy (TEM, JEOL-2100F), atomic force microscopy (AFM, Bruker Germany), X-ray diffraction spectra (XRD, Rinku-Miniflex 600 instrument), X-ray photoelectron spectra (XPS, Phi 5000 Versa Probe Scanning ESCA Microprobe spectrometer), Raman spectra (LabRAM HR 800 Raman spectrometer), UV–vis spectrophotometer (Puxi, TU-1901), and nitrogen sorption measurements (Autosorb 6B).

The cyclic voltammetry, galvanostatic charge-discharge tests, and electrochemical impedance spectroscopy (EIS) were performed using an electrochemical workstation (CHI 660D, Chenhua Instruments, China). The voltage, current, and resistance were measured using a multimeter (DMM 7510, Keithley, Cleveland, OH, USA).

2.3. Density functional theory simulation

Geometry optimization and electronic structure calculations with DFT were performed using the VASP program package. The Perdew-Burke-Ernzerh functional of generalized-gradient approximation was used for electron exchange and correlation, and ultrasoft pseudopotentials were used to describe the nuclei-electron interaction. The kinetic energy cutoff for the plane-wave basis set was 500 eV. The force and energy convergence criteria were set to be 0.01 eV/Å and 10^{-5} eV with a vacuum layer larger than 15 Å, respectively.

2.4. Electrochemical calculations

The capacitance values were calculated from the GCD curves using the following equation:

$$C = (I \times \Delta t) / \Delta, \quad (1)$$

where I, Δt, and ΔV are the discharge current, discharge time, and discharge potential range, respectively. The gravimetric (or areal) specific capacitance C_g (or C_A) was calculated as the ratio of the capacitance to the mass of the active material (or area of the electrode/device). The mass of the LIG scraped from the PI substrate was determined using a microbalance. The mass difference of samples before and after ZnP coating determined the amount of ZnP in ZnP@LIG. The gravimetric specific capacitances of LIG, ZnP, and ZnP@LIG electrodes were calculated based on the active mass of the LIG, ZnP, and ZnP@LIG, respectively. The energy and power densities were then evaluated from GCD curves from the following equations:

$$E = \frac{1}{2} \times C_s \times \frac{(\Delta V)^2}{3.6} \quad (2)$$

$$P = \frac{E}{\Delta t} \times 3600 \quad (3)$$

The energy density and power density of the device were calculated based on the active mass of ZnP@LIG of the device.

3. Results and discussion

As depicted in Fig. 1, the all-in-one stretchable MSCAs can be conveniently fabricated by spray coating and anchoring ultrathin ZnP nanosheets synthesized by a solvothermal method on the 3D LIG foam through a shadow mask. In a typical synthesis process (Fig. 1a), the ZnO nanosheet precursors were prepared by fast-heating a homogeneous solution consisting of $Zn(acac)_3$, CTAB, ethylene glycol, and distilled water. Following an in situ phosphorization treatment in an oven at 300 °C for 2 h in a flowing Ar atmosphere with a heating rate of 3 °C/min, centrifuging the mixture and drying in the vacuum oven yielded the ultrathin ZnP nanosheets. Next, the 3D LIG foams in a designed pattern were prepared by in situ scribing of a commercial insulating polyimide (PI) film with a computer-controlled CO_2 laser. The 3D LIG foams exhibited ordered honeycomb-like morphology (Fig. S1, Supporting Information), increasing the specific surface area to facilitate the electrolyte penetration into the active materials. After dispersing the ultrathin ZnP nanosheets in the deionized water, ethanol, and Nafion solution to yield a spray ink, the ink was spray coated on the 3D LIG foam through a shadow mask, followed by the freeze-drying process (Fig. 1b). The mass of ZnP@LIG electrode composites was about 5 mg cm^{-2} with 1.5 mg cm^{-2} LIG and 3.5 mg cm^{-2} ZnP. The sufficiently strong anchoring of ultrathin ZnP nanosheets on the LIG foam was achieved by electrostatic interactions, covalent and hydrogen bonding, or ionic charge transfer [20], which would lead to the following synergistic effects. Firstly, the ultrathin ZnP nanosheets anchored on the 3D LIG foam enhance the mass loading of active materials for high energy density. Secondly, the 3D conductive LIG foam improves electron transport while retaining the ionic conductivity. Lastly, the hydrophilic ZnP nanosheets can improve the surface wettability of the LIG and induce pseudocapacitance in carbon-based LIG nanomaterials. In fact, the contact angle of ca. 35° on ZnP@LIG is significantly reduced from that of ca. 73° on LIG (Fig. S3), suggesting efficient transport of electrolyte ions into the hybridized electrode. Within the ZnP@LIG hybrid electrode, the 3D LIG foam with a relatively low electrical double-layer capacitance exhibits high electrical conductivity and provide short transport lengths for electrons and ions [21,22], whereas the ultrathin ZnP nanosheets offer a high pseudocapacitance for a greatly improved energy density [23]. These synergistic effects account for the enhanced electrochemical capacitive performance observed in the hybrid electrodes. Combining the ZnP@LIG nanocomposite with a small thickness with a solid-state ion-gel electrolyte and a thin layer of PDMS encapsulation results in supercapacitors with excellent mechanical flexibility. Configuring these flexible supercapacitors cells in an islands-bridge layout with serpentine LIG interconnects further yields the all-in-one stretchable MSCAs with serial and parallel configurations for well-controlled output potentials/currents (Fig. 1c).

The optical image of active ZnP@LIG hybrid electrodes clearly shows a dark color compared to the light orange in the PI (Fig. 2a), which is consistent with previously reported results [24]. The scanning electron microscopy (SEM) images of ZnP@LIG indicate ample porosity in the porous networks with crumpled graphene framework and ultrathin ZnP nanosheets (Fig. 2b–d). The spacing between porous fingers with a width of 1600 μm and an average thickness of 100 μm in the interdigitated electrode is ca. 350 μm (Fig. S1, Supporting Information). In addition, the morphology of the ZnP nanosheets has also

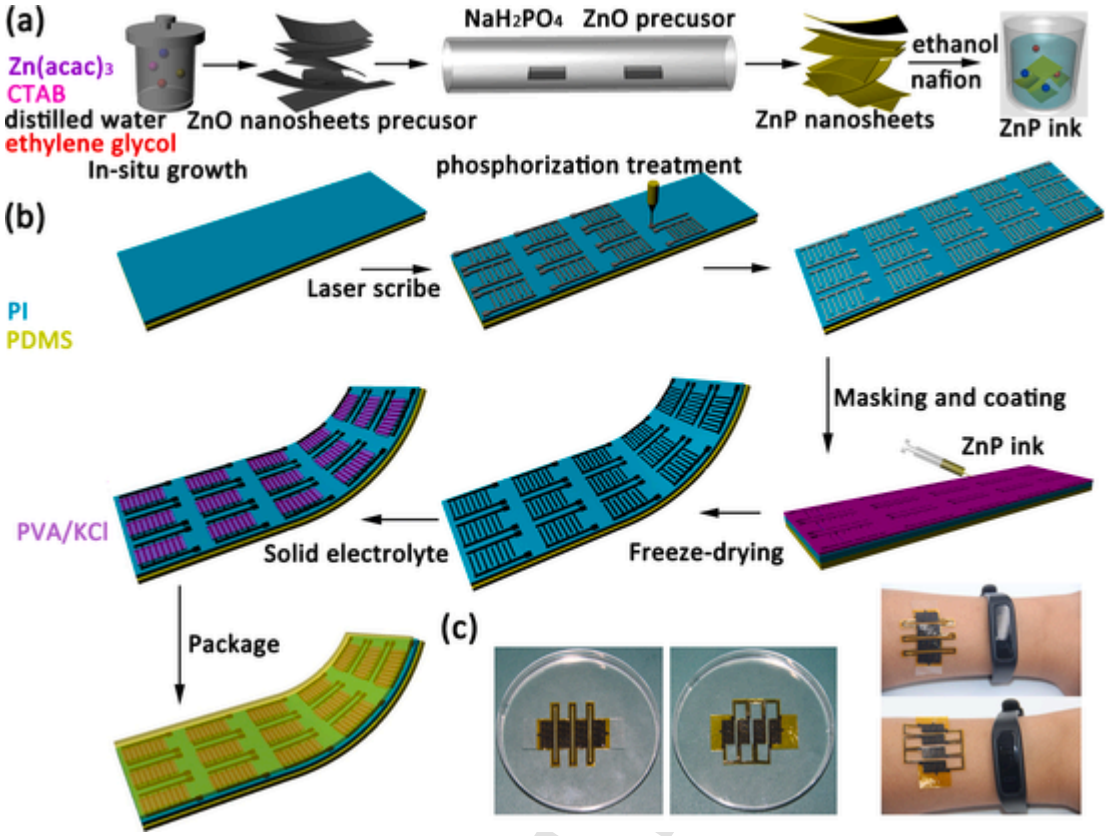

Fig. 1. Synthesis process and optical images of an all-in-one stretchable microsupercapacitor arrays (MSCAs) based on hybrid electrodes with ultrathin ZnP nanosheets anchored on 3D laser-induced graphene foams (LIG) configured in an island-bridge layout. (a) Schematic illustration of the synthesis process to prepare ultrathin ZnO and ZnP nanosheets. After synthesizing the ZnO nanosheets by a solvothermal method, they are used as the precursor to synthesize the ultrathin 2D ZnP nanosheets. (b) Schematic to show the preparation process of all-in-one stretchable MSCAs. After creating the 3D LIG foam by pulsed irradiation of polyimide (PI) thin film with a CO_2 laser, spray coating ZnP on the LIG through a shadow mask prepares the ZnP@LIG electrodes, followed by drop-casting of a PVA/KCl gel electrolyte and packaging with a thin layer of polydimethylsiloxane (PDMS). (c) Optical images of all-in-one stretchable MSCAs connected in serial and parallel configurations in the petri dish (left) and on the human subject (right).

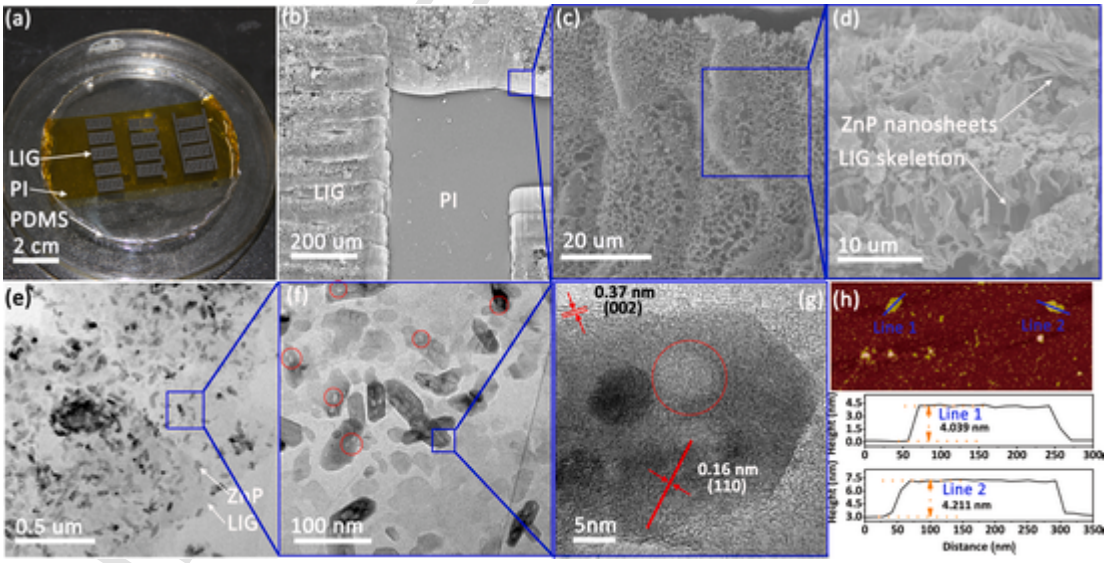

Fig. 2. Morphological and structural characterizations of ZnP@LIG nanocomposite. (a) Optical image of the all-in-one MSCAs based on the ZnP@LIG nanocomposites. (b–d) Scanning electron microscopy (SEM) images, (e and f) transmission electron microscopy (TEM), and (g) high-resolution TEM (HRTEM) images of the ZnP@LIG nanocomposites. (h) Atomic force microscopy (AFM) image and the corresponding height profiles of the ultrathin ZnP nanosheets.

been observed to be unaltered compared to that of the ultrathin nanosheet before phosphorization treatment (Fig. S2, Supporting Information). The transmission electron microscopy (TEM) images of the ZnP@LIG nanocomposite further indicate their relatively uniform pattern of rectangular shape (Fig. 2e–g), which contains a high density of mesopores with an average pore size of ~10 nm as indicated in the high-resolution TEM (HRTEM) images (Fig. 2g). The two lattice spacings of 0.37 and 0.16 nm also correspond to the (002) plane of graphene carbon

and (110) plane of the hexagonal ZnP phase, respectively. As confirmed by the atomic force microscopy (AFM) image and the corresponding height profiles, the smooth ZnP nanosheet has an average thickness of ~4.1 nm (Fig. 2h). The smooth ZnP nanosheet is also observed to anchor on the LIG foam throughout the entire ZnP@LIG nanocomposite, as indicated by the homogenous distribution of Zn, P, and C in the elemental mapping (Fig. S4). Therefore, all of the above results have confirmed the successful integration of the faradaic material (i.e., ultrathin ZnP nanosheets) with 2D capacitive material (i.e., LIG) in the interdigitated electrode.

Compared to that of PI, the X-ray powder diffraction (XRD) pattern of LIG shows an intense peak centered at $2\theta = 24.6^{\circ}$, giving a typical interlayer spacing of ~0.37 nm between the (002) planes in the LIG to suggest a high degree of graphitization (Fig. S7a). At the same time, the typical XRD patterns of ZnO, ZnP, and ZnP@LIG are observed (Fig. 3a), with featured diffraction peaks for the hexagonal wurtzite structure in ZnO crystals (JCPDS card no. 36–1451, space group: *P63mc*(186); $a = b = 3.25$ Å, $c = 5.207$ Å, $\alpha = \beta = 90^{\circ}$, $\gamma = 120^{\circ}$). In contrast, the diffraction peaks in ZnP and ZnP@LIG slightly shift to smaller 2θ angles due to the substitution of P anions with a larger size. The comparison between these XRD patterns in Fig. 3a also confirms the substitution of O atoms in the ZnO matrix with the P atoms in ZnP and ZnP@LIG, while the crystal structure remains unchanged. The energy dispersive spectroscopy (EDS) microanalysis of the ZnP@LIG nanocomposite provides the distribution of the Zn, P, and C elements with the atomic ratio of 24.5: 383.3: 37.2 for Zn: P: C (Fig. S7b), further supporting the successful integration. In addition to the three characteristic peaks at ~1350, 1580 and 2700 cm^{-1} that correspond to defects or bent sp^2 carbon bonds, first-order, and second-order zone-boundary phonons [25], the G/D intensity ratio of ~4.1 in the Raman spectrum of the LIG indicates a high degree of graphene formation (Fig. S7c). The 2D/G intensity ratio of ~0.5 in the Raman spectrum of the LIG also indicates few-layered structures in the laser-induced graphene, consistent with the previous literature reports [26,27]. Because the characteristic peaks of ZnP show a red-shift as compared to that of ZnO, the characteristic peaks of ZnP@LIG below 2000 cm^{-1} in Fig. 3b could be completely indexed to ZnP and graphene, indicating the successful loading of ZnP on the LIG. The valence state elemental composition and variation in the electronic structure after the formation of the ZnP@LIG have further been confirmed by the X-ray photoelectron spectroscopy (XPS) (Fig. 3c–e). The full XPS spectrum of ZnP@LIG confirms the presence of Zn, P, and C elements, consistent with the EDS results (Fig. 3c). As shown in Fig. 3d, the Zn *2p* in ZnP@LIG shows two spin-orbit doublets of Zn $2p_{3/2}$ and Zn $2p_{1/2}$ that correspond to an energy peak of 1021.2 and 1044.3 eV, respectively. After phosphorization, the two peaks shift to lower binding energies of 1020.1 eV (Zn $2p_{3/2}$) and 1043.1 eV (Zn $2p_{1/2}$) with the spin-energy separation changed from 23.0 to 23.1 eV, implying that the density of the electron clouds of Zn atoms decreases. Moreover, three prominent peaks of 126.5, 128.0, and 133.4 eV in the P *2p* spectrum correspond to P $2p_{3/2}$, P $2p_{1/2}$, and P-O (attributed to slight surface oxidation) (at the top of Fig. 3e), respectively. The high-resolution C *1s* in ZnP@LIG fits one major peak at 284.3 eV (corresponding to C—C) and three minor peaks at 285.5, 287.5, and 288.2 eV (corresponding to C—N, C—O, and C═O) (at the bottom of Fig. 3e), suggesting that the LIG is dominated by sp^2-carbons. Additionally, the specific surface area and pore size distributions of the as-prepared samples have been analyzed by carrying out nitrogen adsorption/desorption characterizations based on Brunauer-Emmett-Teller (BET) and Barrett-Joyner-Halenda (BJH) methods (Fig. 3f). While the LIG has a specific surface area of ~320 $m^2\ g^{-1}$ by BET with an average diameter of 374 nm, the ZnP@LIG exhibits a slightly higher specific surface area of ~345 $m^2\ g^{-1}$ and a larger average diameter of 435 nm, likely attributed to the existing pores in the ultrathin ZnP nanosheets. These observations would promise the enhanced ionic conductivity of the ZnP@LIG nanocomposite for improved performance of the electrode.

Because the electrical conductivity in crystalline solids mainly depends on their electronic structure, the electronic structures of ZnP and ZnO nanosheets have been investigated by first-principles calculations based on density functional theory (DFT) and UV–vis absorption spectra. The results would help reveal the underlying mechanism of the enhanced electrochemical performance in ultrathin ZnP nanosheets compared to that of ZnO nanosheets. With a direct band-gap of 4.3 eV at the Γ points, ultrathin ZnO nanosheets show a semiconducting nature (Fig. 4a). Flat valence band maximum (VBM) and conduction band minimum (CBM) dispersion along with the high-symmetry lines in

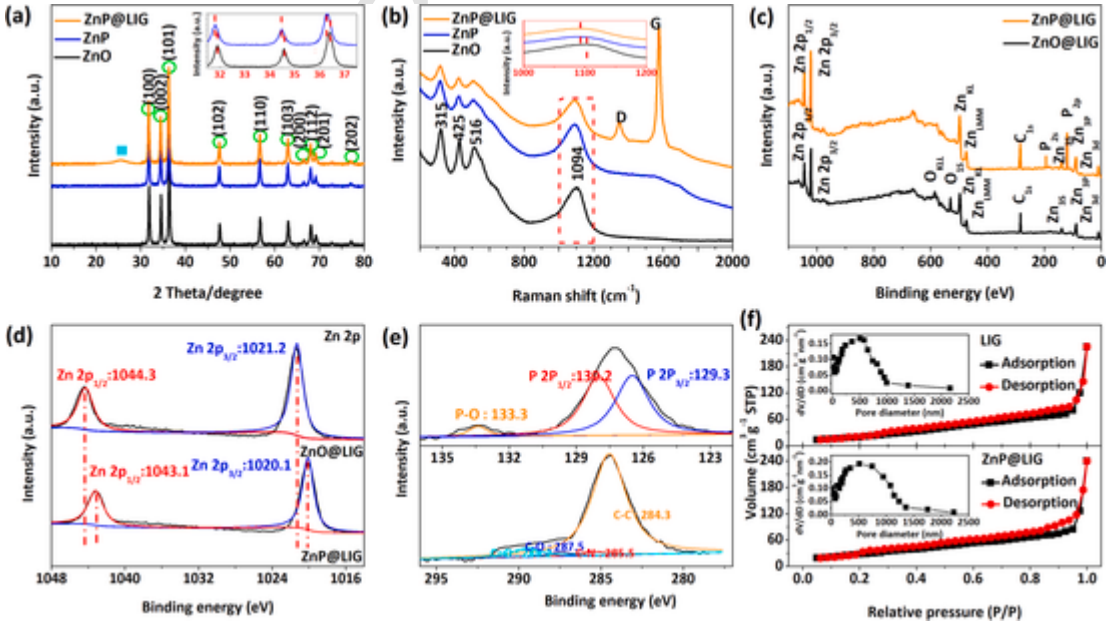

Fig. 3. Structural and electronic properties of ZnP@LIG nanocomposite. (a) X-ray powder diffraction (XRD) and (b) Raman spectra of ZnO, ZnP, and ZnP@LIG. (c) Full survey X-ray photoelectron spectroscopy (XPS) spectra of ZnP@LIG, and ZnO@LIG. (d) High-resolution Zn *2p* of the ZnO@LIG and ZnP@LIG film. (e) High-resolution P *2p* and C *1s* XPS spectra of the ZnP@LIG. (f) N_2 adsorption-desorption isotherms of the LIG and ZnP@LIG, with the corresponding pore size distributions shown in the insets.

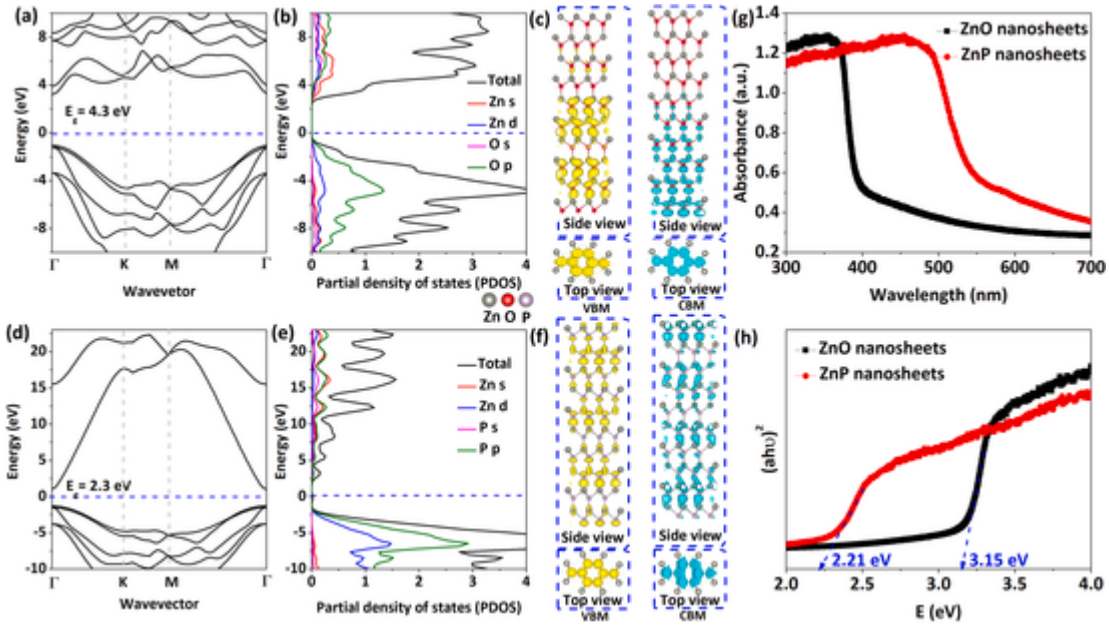

Fig. 4. Electronic structure and UV–vis absorption spectra of ZnO and ZnP nanosheets, showing the phosphorization treatment enhances electronic conductivity for improved electrochemical capacity performance. (a, d) Calculated band structures, (b, e) partial density of states (PDOS), and (c, f) corresponding charge density distributions of conduction band minimum (CBM) and valence band maximum (VBM) at Γ points in (a–c) ZnO nanosheets and (d–f) ZnP nanosheets. (g) UV–vis absorption spectra of ZnO and ZnP nanosheets and (h) the determination of the absorption edges of the samples.

the first Brillion zone strongly indicate the large effective mass of electrons and holes, which would lead to reduced mobility and negatively affect the electronic conductivity [28]. From the partial density of states, O-*2p* and Zn-*4s* mainly contribute to the valence band states and the conduction band states near the Fermi level (Fig. 4b). Furthermore, the charge density distribution of VBM and CBM localized at the bottom edge suggests that it is challenging for the electrons of the valence band to transit into the conduction band in the total width of the nanosheet. When it comes to the hexagonal wurtzite ZnP nanosheets, the band-gap decreases by ~53% to 2.3 eV at the Γ point to facilitate the electron transfer process between the electrode surface and adsorbed electrolyte ions. Different from the flat shape in ZnO, the electronic bands near the Fermi level in ZnP are very dispersive (i.e., parabolic shape) along the high-symmetry lines in the first Brillion zone, implying smaller effective masses of the charge carriers for enhanced mobility. The nonlocalized charge density distributions of VBM and CBM also suggest that the electrical conductivity of ZnP can be notably enhanced. These calculated electronic structure data have been further validated by the UV–vis absorption spectra of ZnO and ZnP nanosheets, with reasonably well agreement. The adsorption stooping edges of ZnP nanosheets with an obvious redshift of ~105 nm from ZnP indicate that the band-gap of ZnP nanosheets is smaller than that of ZnO nanosheets (Fig. 4g). Furthermore, the band-gap of the ZnP and ZnO nanosheets can be established according to Tauc's equation:

$$\left[F(R)^{*}h\nu\right]^{1/2} = A\left(h\nu - E_g\right) \tag{4}$$

where $F(R)$ is the measured adsorption coefficient, E_g is the band-gap width, and A is a constant depending on the transition probability. The approximate linear extrapolation gives the band-gaps of 2.21 and 3.15 eV for the ZnP and ZnO nanosheets, respectively (Fig. 4h) (Although the experimental band-gaps of the ZnP and ZnO obtained from optical absorption spectra were smaller than that of the calculated values due to the intrinsic limitations of DFT method, both theoretical and experimental studies have confirmed that in situ phosphorization treatment can significantly decrease the band-gap of ultrathin nanosheet samples). These results strongly suggest that in situ phosphorization treatment of ZnO to form ultrathin ZnP nanosheets can significantly decrease the band-gap, leading to improved electric conducting properties.

The electrolyte ions adsorption energy on electrodes is another critical factor to dictate the number of adsorbed charged ions at the electrode surface during the charging process. Therefore, the adsorption energies of Na^+ and K^+ on the surfaces of ZnO(001) and ZnP(001) nanosheet ($-\Delta G_M$, M = Na or K) have been calculated at room temperature (T = 298 K) from the following formula:

$$\Delta G_M = E_M + \Delta E_{ZPE} - \mathrm{E_M\,(sold)} - T\Delta S - 0.059\,pH \tag{5}$$

where E_M, ΔE_{ZPE}, E_M(solid), and ΔS are the calculated energies of M atom, zero-point energy (ZPE), total energies of M solid, and the difference of entropy between the adsorbed state, and the free-standing state, respectively. The adsorption energies of K^+ and Na^+ on ZnP(001) (i.e., $-\Delta G_K = -3.37$ eV; $-\Delta G_{Na} = -3.12$ eV) are much larger than those of on ZnO(001) (i.e., $-\Delta G_K = -2.95$ eV; $-\Delta G_{Na} = -2.77$ eV) (Fig. S3, Supporting Information). Because larger negative adsorption energy means a stronger binding, it could be easier for ZnP to absorb and store more electrolyte ions at the electrode surface for significantly improved specific capacitance and energy density [29]. The above results all indicate that our newly developed ultrathin ZnP nanosheets would be an excellent candidate of active faradaic materials for hybrid electrodes due to the increased conductivity and number of adsorbed electrolyte ions compared to ZnO nanosheets.

The investigation of the electrochemical performance of the ZnP@LIG nanocomposite involves the use of a three-electrode electrochemical system with Na_2SO_4 aqueous solution of 0.5 M as the electrolyte. Compared to the cyclic voltammetry (CV) behavior of LIG at different scan rates (10–100 mV s^{-1}) (Fig. 5a), the loading of ultrathin ZnP nanosheets in ZnP@LIG nanocomposite significantly increases the current response in CV curves (Fig. 5b). The CV curves of the ZnP@LIG nanocomposite clearly reveal the pseudocapacitive features with pronounced redox peaks due to the reversible redox reactions at the surface of the ZnP ultrathin nanosheets. Generally speaking, the charge storage mechanisms of the transition-metal compound mainly depend on the insertion/extraction of protons and/or electrolyte ions, as well as the transitions between different valence states of the transi-

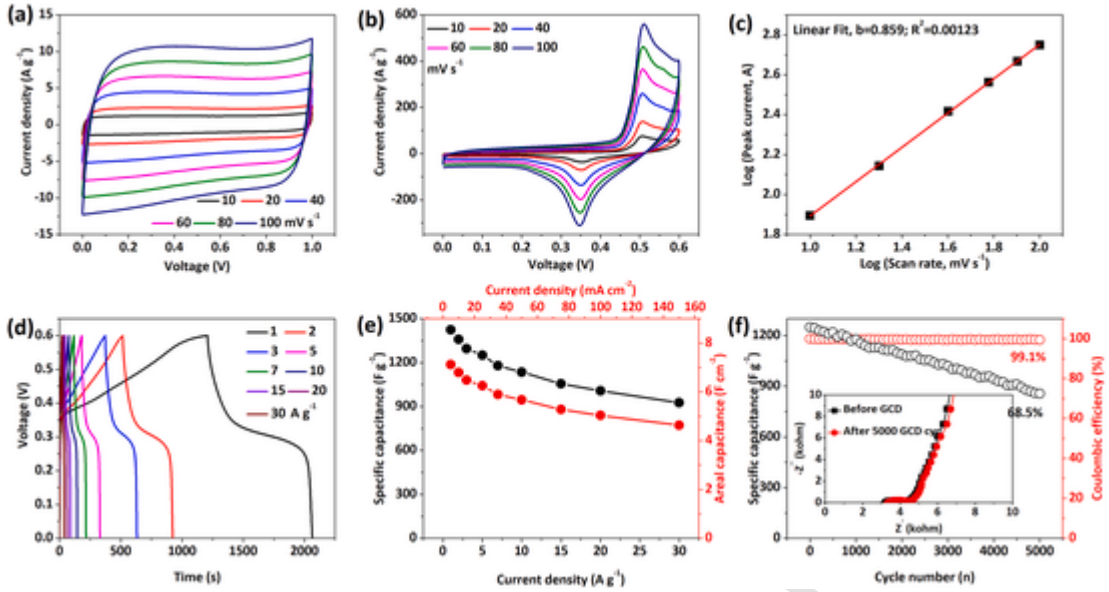

Fig. 5. Electrochemical performance of the ZnP@LIG electrode. CV curves of (a) the LIG and (b) ZnP@LIG electrodes at the scan rate of 10–100 mV s^{-1}. (c) Logarithm peak current response plotted against the logarithm scan rate of the ZnP@LIG electrode at different scan rates. (d) Galvanostatic charge-discharge (GCD) curves of ZnP@LIG electrodes at the current densities from 1 to 30 A g^{-1}. (e) The specific gravimetric capacitance and areal capacitance of ZnP@LIG at current densities of 1–30 A g^{-1}. (f) Cycling stability and Coulombic efficiency of the ZnP@LIG at 3 A g^{-1} for 5000 cycles, with the corresponding electrochemical impedance spectra (EIS) before and after 5000 cycles shown in the inset.

tion-metal compound. Thus, the electrochemical reaction of ZnP with the NaSO4 electrolyte can be assumed to follow $(ZnP)_{surface} + Na^+ + e^- \leftrightarrow (ZnP—Na^+)_{surface}$ in a simplified view. The experimental confirmation of this mechanism is yet to be investigated in future works. The current densities of both LIG and ZnP@LIG electrodes increase with the increasing scan rate as expected, indicating low charge-transfer resistances and a high rate capability performance. The charge storage mechanism of the ZnP@LIG nanocomposite can also be understood from the linear relationship between the peak current density and scan rate (Fig. 5c). According to the previous reports [30], the contribution of capacitive- and diffusion-controlled charge of the electrode can be calculated from $i = av^b$, where $b = 0.5$ for a diffusion-controlled process and $b = 1$ for a surface capacitive-controlled process. The value of $b = 0.859$ in the ZnP@LIG nanocomposite is closer to 1, implying the diffusion-dominated charge storage behavior (Fig. 5c). The galvanostatic charge-discharge (GCD) tests have also been carried out for the LIG (Fig. S8a) and ZnP@LIG (Fig. 5d) electrodes at different current densities (from 1 to 30 A g^{-1}). The nearly symmetric triangular profiles observed in the GCD curves of the LIG are indicative of excellent capacitive behavior and Coulombic efficiency of 99.85% at 1 A g^{-1} (Fig. S8a). In comparison, well-defined voltage plateaus in the relatively symmetric charge-discharge GCD curves of the ZnP@LIG electrode could contribute to increased capacitance values (Fig. 5d). The well-maintained voltage plateau in the GCD curve even at a high charge-discharge current density of 30 A g^{-1} implies the highly efficient ion diffusion in the ZnP@LIG nanocomposite due to the mesoporous channel with micropores. Derived from the GCD curves, the specific capacitance versus discharge current density can be calculated for the LIG and ZnP@LIG electrodes. The specific gravimetric (areal) capacitance of the LIG could deliver 115 F g^{-1} (or 0.1725 F cm^{-2}) at 1 A g^{-1} (or 1.5 mA cm^{-2}), with 74.6% maintained (i.e., 85 F g^{-1} or 0.1275 F cm^{-2}) even at 30 A g^{-1} (or 45 mA cm^{-2}) (Fig. S8b). Benefiting from the pseudocapacitive ultrathin ZnP nanosheets and free electrolyte transport channels, the ZnP@LIG nanocomposite with interconnected pores exhibit drastically improved charge storage behavior compared to that of the LIG. As the current density ranges from 1 to 30 A g^{-1} the gravimetric (areal) capacitance of the ZnP@LIG nanocomposite electrode gradually decreases from 1425 F g^{-1} (or 7.125 F cm^{-2}) to 926 F g^{-1} (or 4.631 F cm^{-2}) (Fig. 5e). Although capacitance retention of 65.0% in ZnP@LIG is smaller than that of LIG, its gravimetric (areal) capacitance is still over 10 times than that of the LIG. The impressive capacitive behavior of the ZnP@LIG is likely attributed to the combined storage mechanisms of the pseudocapacitive ZnP nanosheets for faradaic and the conductive 3D LIG foam for capacitive storage. The above results confirm the high specific capacitance and remarkable rate capability in the ZnP@LIG electrode.

The cycling stability of LIG and ZnP@LIG electrodes has also been measured by the GCD technique at a current density of 3 A g^{-1} over 5000 cycles. While the capacitance retention of 68.5% in the ZnP@LIG electrode after 5000 charge-discharge cycles (Fig. 5f) is smaller than 91.8% in the LIG electrode (Fig. S8c), its gravimetric (areal) capacitance is still ~8.8 times higher than that of the LIG. At the same time, both the LIG and ZnP@LIG electrodes exhibit superior Coulombic efficiency of 99.4% and 99.1% after cyclic 5000 charge-discharge cycles (Figs. S8c and 5f). As shown in the inset of Figs. S8c and 5f, the Nyquist plots of the LIG and ZnP@LIG electrodes before and after charge-discharge cycles display small impedance arcs in the high-frequency region and small intercept along Z′, indicating low charge-transfer resistance (R_{ct}) and equivalent series resistance (R_s). Only a small increase in resistances for both electrodes after 5000 cycles further demonstrate high conductivity and short electrons/ions transport pathways for good cycling performance.

Motivated by the excellent capacitive behavior of the electrochemical performance of ZnP@LIG shown in half-cells, we combine the ZnP@LIG with PVA/KCl gel electrolyte into an all-in-one planar MSC configured in an island-bridge layout (Fig. 6). The as-assembled all-in-one planar MSC has a mass loading of 10 mg cm^{-2} and a thickness of 110 μm (including a thin PVA/KCl gel electrolyte film with a thickness of 10 μm drop-cast on the MSC islands for ionic transport). CV curves in the scan range between 5 and 30 mV s^{-1} for a voltage from 0 to 0.6 V show quasi-rectangle shape without distinct redox peaks (Fig. 6a). The resulting shapes may be attributed to the comparable capacitances between the one arising from the double-layer capacitance of the interconnected porous hybrid nanostructures and the redox pseudocapacitance of the ZnP in the all-solid supercapacitor [21]. Moreover, the diffusive (or pseudocapacitance) and capacitive (or electrical double-

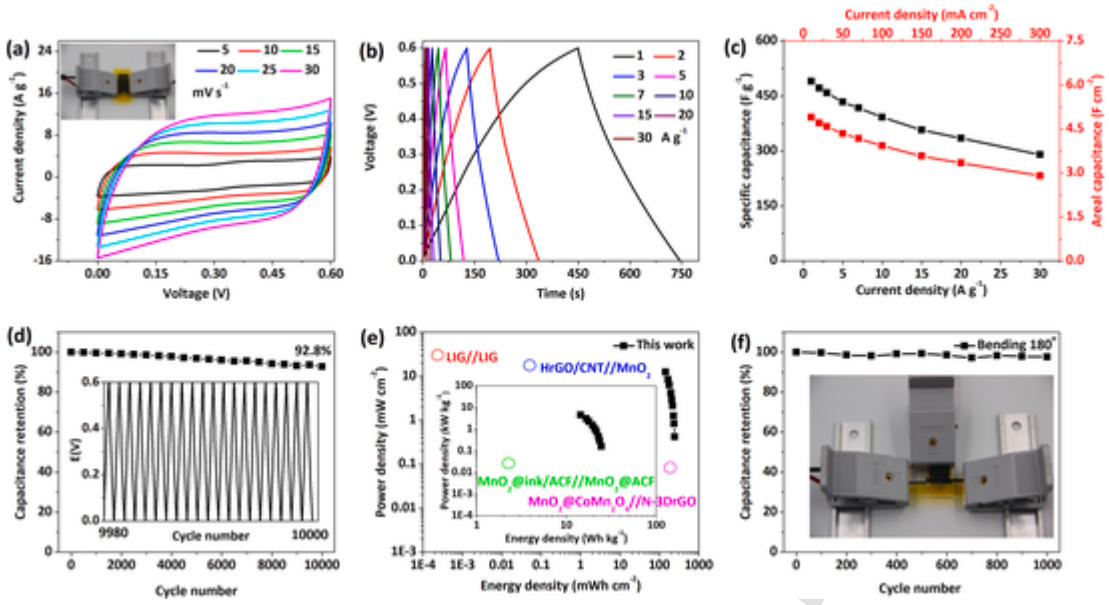

Fig. 6. Electrochemical performance of an all-in-one planar MSC based on ZnP@LIG electrodes configured in an island-bridge layout. (a) CV curves of the all-in-one planar MSC at the scan rate from 5 to 30 mV s^{-1}, with an optical image shown in the inset. (b) GCD curves at current densities from 1 to 30 A g^{-1}. (c) The specific gravimetric capacitance and areal capacitance at different current densities. (d) Cycling stability at 3 A g^{-1} for 10,000 cycles. (e) Ragone plots that compare the energy and power densities from this work with those in the literature reports. (f) The capacitance retention versus bending cycles at a bending angle of 180°, with an optical image of the testing setup.

layer capacitors, EDLCs) contributions of the device at a fixed scan rate can be separated by fitting the CV data with the power law [30] of $i(V) = k_1\nu + k_2\nu^{1/2}$, with the first and second terms for the capacitive- and diffusion- controlled currents. At a scan rate of 5 mV^{-1}, the current density with a capacitive contribution ratio of 54.7% (capacitive current response in the shaded area) is slightly dominated by the capacitive-controlled process, confirming the synergistic combination of capacitive and faradaic storage mechanisms in one device (Fig. S9a). As the scan rate increases from 5 to 50 mV s^{-1}, the capacitive contribution ratio slowly increases from 54.7% to 63.7% (Fig. S9b).

As the current density increases from 1 to 30 A g^{-1}, the GCD curves of the all-in-one planar MSC exhibit distorted voltage-time profiles for the charging and discharging process, suggesting that ultrathin ZnP nanosheets loaded in the 3D LIG foam contribute to efficient faradaic reactions for energy storage (Fig. 6b). Calculated from the GCD curves at different current densities, the specific gravimetric (areal) capacitance of our device could achieve 490 F g^{-1} (or 4.9 F cm^{-2}), 434 F g^{-1} (or 4.34 F cm^{-2}), 392 F g^{-1} (or 3.92 F cm^{-2}), 357 F g^{-1} (or 3.57 F cm^{-2}), 334 F g^{-1} (or 3.34 F cm^{-2}), 290 F g^{-1} (or 2.90 F cm^{-2}) at the current densities of 1, 5, 10, 15, 20, 30 A g^{-1}, respectively (Fig. 6c). This specific capacitance is far higher than those of previously reported MSCs, including oxygen-rich carbon nanosheets (CNSs)//framework carbon derived activated carbon (FCDAC) (192 F g^{-1} at 0.5 A g^{-1}) [31], MXene-N//MXene-N (70.1 mF cm^{-2} at 10 mV s^{-1}) [32], graphene oxide/commercial pen ink//graphene oxide/commercial pen ink (15.57 μF cm^{-2} at 0.1 μA) [33], nanoporous gold/MnO_2//nanoporous gold/MnO_2 (170 F g^{-1} at 20 A g^{-1}) [34], among others. The Nyquist plot of the MSCs shows a near semi-circular shape in the high to medium frequency region, a low intercept along Z′, and a straight line in the low-frequency region (Fig. S10). The equivalent circuit in Fig. S10b results in a charge transfer resistance R_{ct} of 17.4 Ω, an equivalent series resistance R_S of 6.0 Ω, and an electrolyte/proton diffusion resistance W of 25.5 Ω. The obtained values indicate low resistance and fast ion transport in the all-solid-state MSCs for enhanced electrochemical performance. Moreover, the excellent cyclic stability of the as-assembled all-in-one planar MSCs has been demonstrated with capacitance retention of ~92.8% after 10,000 cycles at 3 A g^{-1} (Fig. 6d). Evaluation of the energy and power densities of the all-in-one MSCs based on the total electrochemically active electrode areas (masses) in the Ragone plot indicates the highest areal (gravimetric) energy density 245 m Wh cm^{-2} (or 24.5 Wh kg^{-1}) at a power density of 0.4167 mW kg^{-1} (or 0.1581 kW kg^{-1}) (Fig. 6e). Our device could also maintain an energy density of 145 m Wh cm^{-2} (or 14.5 Wh kg^{-1}) at a power density of 12.5043 mW kg^{-1} (or 4.5 kW kg^{-1}). These results are clearly higher than previously reported all-solid-state supercapacitors based on LIG//LIG (30 mW cm^{-2} at 0.2 μWh cm^{-2}) [12], MnO_2@$CoMn_2O_4$//N-3DrGO [28], HrGO/CNT//MnO_2 (106.2 μWh cm^{-2}) [35], MnO_2@ink/ACF//MnO_2@ACF (70 μWh cm^{-2} at 900 μW cm^{-2}) [36], among others.

In addition to their excellent electrochemical performance, the prepared devices with superior mechanical properties are also highly flexible to be compatible for integration with flexible electronics. The bending of 180° only results in a negligibly small capacitance decay of 0.3% (Fig. 6f). Capacitance retention of > 97.6% is still achieved even after a bending cycle of 1000 times. The excellent flexibility of the all-in-one MSCs originates from the small thickness in the all-in-one device architecture to drastically reduce the bending stiffness of the hybrid electrode materials in the device [37]. Moreover, the maximum bending strain in the device is also reduced because it is linearly proportional to the thickness of the device. The elimination of the multilayer design also avoids the possible concern for delamination between layers, which partly alleviates the volume change induced by faradaic reactions during the charging-discharging process as well.

To meet specific output voltage/current needs for practical applications, four all-in-one planar MSCs have been demonstrated in series (Fig. 7a) and parallel (Fig. 7b) connections with an island-bridge layout. Compared to a single MSC with an output voltage of 0.6 V, the MSCAs connected in series demonstrate a four-time increase in the output voltage to 2.4 V, as expected (Fig. 7c and e). Meanwhile, MSCAs connected in parallel generate a four-time output in the current density while maintaining the same output voltage of 0.6 V in the charging-discharging process (Fig. 7d and f). Moreover, the serial or parallel connections in the MSCs can be easily scaled up, as shown in a proof-of-concept demonstration with up to 20 MSCs (Fig. 7g). The linear relationship between the overall capacitance of the assembled all-in-one planar MSCAs and the number of devices in the array clearly showcases excellent performance uniformity and scalability.

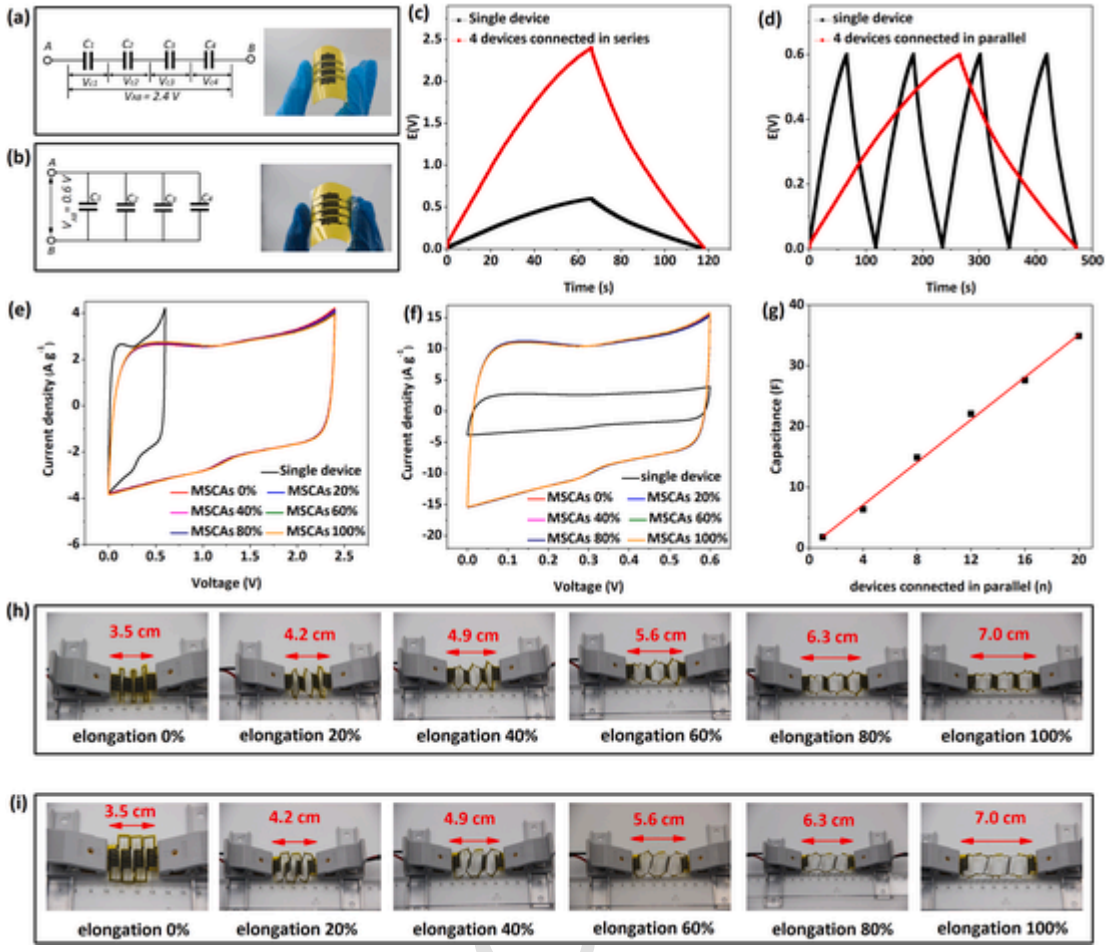

Fig. 7. Electrochemical and mechanical properties of the all-in-one planar MSCAs with serial and parallel connections. The equivalent circuit diagrams and photographs of the four devices connected in (a) series and (b) parallel. GCD curves of the four devices in (c) serial and (d) parallel connections at a current density of 5 A g^{-1}. Real-time collected CV curves of single devices and the all-in-one MSCAs with (e) serial and (f) parallel connections under an applied strain ranging from 0% to 100% elongation. (g) The relationship between the overall capacitance from the all-in-one MSCAs and the number of devices connected in parallel. (h–i) Real-time images of as-obtained all-in-one stretchable MSCAs comprised of four devices interconnected in (h) series and (i) parallel configurations upon a tensile strain up to 100%.

In addition to serve as a means for serial/parallel connections, the wavy interconnects also provide the all-in-one MSCAs with excellent stretchable properties. In the all-in-one stretchable planar MSCAs, the interdigital electrodes with as-prepared ZnP@LIG nanocomposite in the PDMS act as energy storage functional islands and do not experience substantial tensile deformation during stretching. In contrast, the wavy LIG interconnects act as a bridge to connect energy storage functional islands, which can unfold and follow the applied tensile strains through out-of-plane buckling and twisting [38]. Therefore, the real-time images of as-obtained all-in-one stretchable MSCAs comprised of four devices interconnected in serial (Fig. 7h) and parallel (Fig. 7i) can be stretched up to a tensile strain of 100%, with negligible changes in the corresponding CV responses (Fig. 7e and f). The high capacitance retention performance of 97.5% and 97.2% has also been measured in the all-in-one stretchable MSCAs connected in serial and parallel for a tensile strain of 100% (Fig. S4, Supporting Information). These results highlight that the all-in-one stretchable MSCAs can achieve a high mechanical stretchability with adjustable voltage and current outputs to meet different requirements in the practical applications of wearable electronics. To the best of our knowledge, the newly developed and demonstrated all-in-one stretchable MSCAs with excellent mechanical stretchability and capacitance performance are among the best and compare favorably with those reported previously (Table 1).

As a proof-of-the-concept demonstration toward the self-powered stretchable and wearable system, the all-in-one stretchable MSCAs have been integrated with a crumpled Au-based triboelectric nanogenerator (TENG) and a crumpled graphene-based stretchable strain sensor. In such a system, the all-in-one stretchable MSCAs efficiently charged by the crumpled Au-based TENG provide power for the stretchable crumpled graphene-based strain sensor on a very-high-bond (VHB) substrate. The TENG consists of a triboelectric layer with crumpled Au on PDMS and a collecting electrode with the PDMS/Au composite (Fig. 8a), as in our previous work [47]. The contact-electrification and electrostatic-induction process account for the power generation in the crumpled Au-based TENG (see details in Fig. S5, Supporting Information). The performance of the crumpled Au-based TENG has been characterized at different frequencies from 10 to 100 Hz (driven by an external force supported by a shaker motor) for a load resistance of 1 MΩ. The output voltage increases with the increasing frequency in the frequency range from 10 to 80 Hz, because the consecutive contact–separation of the surfaces at a higher frequency would lead to a larger amount of transferred charges (Fig. 8b and Fig. S6a, Supporting Information). However, the output voltage decreases as the frequency increases from 80 to 100 Hz, which is attributed to the significantly decreased transferred charge density as the compressive force is not fully released. Meanwhile, the dependence of the output current on the fre-

Table 1
Comparison of the specific areal capacitance, elongation, testing condition, and mass loading between our all-in-one stretchable MSCAs and recently reported stretchable MSCs.

Electrode materials	Areal capacitance (mF cm $^{-2}$)	Elongation (%)	Testing conditions	Mass loading (mg cm $^{-2}$)	Ref.
ZnP@LIG	2900	100	5 mA cm $^{-2}$	10	This work
MWCNT/PANI	44.13	40	0.2 mA cm $^{-2}$	–	[39]
Polypyrrole/CNT	5.17	30			[40]
Few-layered MXene flake	111.5	100	5 mA cm $^{-2}$	2.0	[10]
MXene/BC@PPy	200.47	200	7.5 mA cm $^{-2}$	9.56	[41]
SWCNTs	0.74	30	7.5 mA cm $^{-2}$	0.3	[42]
MWCNT/Mn_3O_4	0.4895	50			[43]
rGO	0.54	100	500 mV s $^{-1}$	–	[44]
MWCNT/Mn_3O_4	0.57	40	0.1 A cm $^{-3}$	6	[45]
MWNTs	0.51	80	0.006 mA cm $^{-2}$		[46]

quency shows a similar trend, with 9.9 μA at 10 Hz and 16.0 μA at 80 Hz (Fig. S6b, Supporting Information). These results indicate that the optimal driving frequency for our crumpled Au-based TENG is 80 Hz. Next, the output power of the crumpled Au-based TENG is evaluated by connecting it with different external load resistances ranging from 10 kΩ to 10,000 MΩ (Fig. S6c, Supporting Information). The output power first increases and then decreases with the increasing resistance in the external load, with the maximum output power of 0.192 mW for a load of 2 MΩ. The output performance of the crumpled Au-based TENG remains relatively stable over 16,000 contact and separation cycles and demonstrates excellent stability, which results from the robust PDMS coating with good durability and flexibility (Fig. S6d, Supporting Information). It is worth to note that the output voltage and current density exhibit a huge increase for the improved overall output performance as the tensile strain of 100% is applied (Fig. S7, Supporting Information), due to the increased contact area in the crumpled-Au film from the applied tensile strain. This result highlights the potential for the crumpled Au-based TENG to power stretchable sensors and to charge stretchable energy storage devices such as the all-in-one stretchable MSCAs.

The feasibility to charge the all-in-one stretchable MSCAs with the crumpled Au-based TENG is further demonstrated. The stretchable MSCAs with a different number of MSCs connected in parallel are charged by the rectified output of the crumpled Au-based TENG driven by a shaking motor at 80 Hz, with the charging curves presented in Fig. 8c. The voltages of the single MSC and MSCAs all increase steadily with the charged time, indicating the stable and durable output from the Au-based TENG. For the single MSC, it only takes 60 s for the voltage to increase from 0 to 0.6 V (Fig. 8c), and then 48 s to discharge at a current of 1 mA (Fig. S8a, Supporting Information). In the case of all-in-one stretchable MSCAs with different numbers of MSCs, the charging and discharging times increase linearly to further confirm the stable and continuous output from the crumpled Au-based TENG (Fig. S8bc, Supporting Information).

The resistive strain sensor based on crumpled graphene can be easily fabricated with a pre-strain strategy according to our previous work [48]. Briefly, after attaching the graphene on a uniaxially pre-stretched VHB film, the release of the pre-strain forms crumpled graphene. Following the wire connection to the fully charged all-in-one stretchable MSCAs as the energy source, encapsulation with another thin VHB layer results in the resistive strain sensor based on crumpled graphene (see the details of the experiment in Figs. S9 and S10, Supporting Information). Compared to the planar graphene film with a maximum tensile strain of only 10%, the crumpled graphene sensor can be stretched to a maximum strain of 210% for a pre-strain of 400% (Fig. S9b, Supporting Information). While the initial resistance (R_0) of the crumpled graphene sensor decrease from 73.2 kΩ to 16.0 kΩ (Fig. S9c, Supporting Information), the normalized resistance change ($\Delta R/R_0$) versus the applied strain (ε) obtained from the electromechanical char-

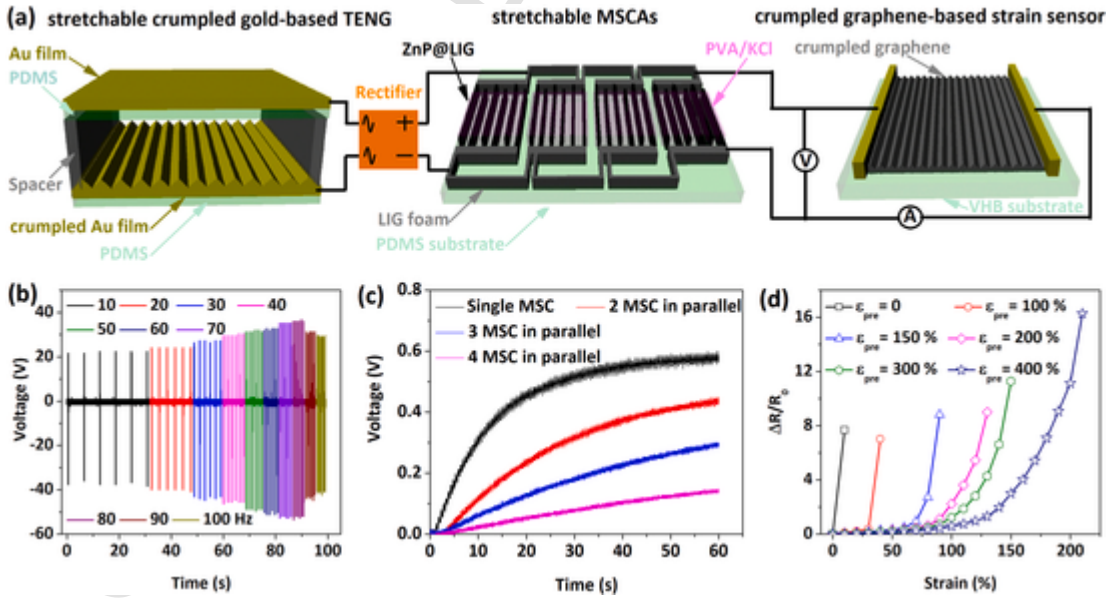

Fig. 8. A self-powered system that integrates as-prepared stretchable MSCAs with a crumpled Au-based triboelectric nanogenerator (TENG) and a crumpled graphene-based stretchable strain sensor. (a) Schematic of the stretchable MSCAs charged by the crumpled Au-based TENG to power the stretchable crumpled graphene-based strain sensor. (b) The measured output voltage of the crumpled Au-based TENG at various frequencies, showing the optimal driving frequency of 80 Hz. (c) Charging curves of our stretchable MSCAs with different numbers of MSCs connected in parallel charged by the crumpled Au-based TENG. (d) The electromechanical characterization of the stretchable strain sensor driven by the as-prepared MSCAs shows the normalized resistance change as a function of the applied strain for various levels of the pre-strain.

acterization of the stretchable strain sensor follows the "J"-shaped curve (Fig. 8d), consistent with the literature reports [49]. Moreover, the curve is similar to that operated with a battery (Fig. S22), indicating that the MSCAs charged by the crumpled Au-based TENG are suitable to operate stretchable devices (e.g., the strain sensor). As the sensitivity of the strain sensor is defined by its gauge factor (GF) that is the ratio of $\Delta R/R_0$ to ε, the GF of the crumpled graphene strain sensor increases from 21.3 to 353.6 as the applied strains increases from below 128% to above for a pre-strain of 400%. While the strain sensor is fully reversible with negligible hysteresis (Fig. S11, Supporting Information) for an applied strain smaller than 128%, it becomes nonreversible in the larger strain range (i.e., > 128%), due to extensive cracks formation on the graphene film. Furthermore, with the strain isolation strategy [50], the MSCAs charged by the crumpled Au-based TENG can be integrated with a graphene-based strain sensor on a single stretchable substrate (e.g., Ecoflex) as a wearable self-powered system for practical application (Fig. S21). These results suggest that the all-in-one stretchable MSCAs can be used to power a stretchable strain sensor with ultra-high sensitivity in a fully integrated manner for self-powered stretchable systems.

4. Conclusions

In summary, a highly porous hybrid nanostructure with non-layered pseudocapacitive ultrathin ZnP nanosheets decorated on 3D laser-induced graphene foams has been successfully prepared through low-cost laser irradiation and a simple spray coating method. The ZnP@LIG hybrid electrodes showcase superior electrochemical performance with a high capacity of 1425 F g^{-1} at 1 A g^{-1} and 926 F g^{-1} at 30 A g^{-1}, along with a capacity retention of 68.5% over 5000 cycles in the Na_2SO_4 aqueous solution electrolyte. The first-principles calculations, together with UV–vis absorption spectra, reveal that the phosphorization treatment of ZnO into ZnP decreases the band-gap and increases the adsorption energy of electrolyte ions. The greatly enhanced electrical conductivity and the number of adsorbed charged ions contribute to the improved rate capability and overall energy density of the electrodes. Moreover, configuring planar MSCs in serial/parallel with the island-bridge layout results in the all-in-one stretchable planar MSCAs with superior energy density and tailored voltage/current outputs, which is stable against bending and stretching deformations (up to a tensile strain of 100%). As a proof-of-the-concept demonstration toward the self-powered stretchable systems, the stretchable MSCAs have been integrated with a crumpled Au-based TENG and a crumpled graphene-based stretchable strain sensor. It would be of high interest to develop self-powered systems with all components based on single multifunctional materials. Although there still remains further improvement, the coupled design principle of electronic materials and device architecture has been demonstrated to serve as a powerful toolset for the future development of high-performance stretchable/wearable systems.

Supporting Information

SEM and TEM images of electrode materials, the electrochemical performance of an all-in-one stretchable MSCAs, the working mechanism and output performance of crumpled Au-based TENG, the charging and discharging curves of the as-prepared MSCAs charged by the crumpled Au-based TENG, the schematic of the fabrication process and electromechanical properties of the crumpled graphene-based strain sensor driven by the as-prepared MSCAs.

CRediT authorship contribution statement

Cheng Zhang: Conceptualization, Investigation, Writing - review & editing. **Zhixiang Peng:** Investigation, Data curation. **Chunlei Huang:** Investigation, Data curation. **Bingwen Zhang:** Investigation, Data curation. **Chao Xing:** Investigation, Data curation. **Huamin Chen:** Investigation, Data curation. **Huanyu Cheng:** Conceptualization, Investigation, Writing - review & editing. **Jun Wang:** Investigation, Data curation. **Shaolong Tang:** Investigation, Data curation.

Declaration of Competing Interest

The authors declare that they have no known competing financial interests or personal relationships that could have appeared to influence the work reported in this paper.

Acknowledgment

This work is supported by the National Natural Science Foundation of China (No. 52002162, 11674185, 21763007), and the Educational Commission of Fujian Province for Youths (Grant No. JAT190640). H.C. would like to acknowledge the supports from the National Science Foundation (NSF) (Grant No. ECCS-1933072), the National Heart, Lung, and Blood Institute of the National Institutes of Health under Award Number R61HL154215, and Penn State University.

Conflict of interest

The authors declare no competing financial interest.

Appendix A. Supporting information

Supplementary data associated with this article can be found in the online version at doi:10.1016/j.nanoen.2020.105609.

References

[1] Y. Qiu, Y. Tian, S. Sun, J. Hu, Y. Wang, Z. Zhang, A. Liu, H. Cheng, W. Gao, W. Zhang, H. Chai, H. Wu, Bioinspired, multifunctional dual-mode pressure sensors as electronic skin for decoding complex loading processes and human motions, Nano Energy 78 (2020) 105337.
[2] N. Yi, H. Cui, L.G. Zhang, H. Cheng, Integration of biological systems with electronic-mechanical assemblies, Acta Biomater. 95 (2019) 91–111.
[3] E. Pomerantseva, F. Bonaccorso, X. Feng, Y. Cui, Y. Gogotsi, Energy storage: the future enabled by nanomaterials, Science 366 (2019) eaan8285.
[4] Y. Jie, J. Ma, Y. Chen, X. Cao, N. Wang, Z.L. Wang, Efficient delivery of power generated by a rotating triboelectric nanogenerator by conjunction of wired and wireless transmissions using Maxwell's displacement currents, Adv. Energy Mater. 8 (2018) 1802084.
[5] Y. Chen, Y. Cheng, Y. Jie, X. Cao, N. Wang, Z.L. Wang, Energy harvesting and wireless power transmission by a hybridized electromagnetic–triboelectric nanogenerator, Energy Environ. Sci. 12 (2019) 2678–2684.
[6] G. Cheng, H. Zheng, F. Yang, L. Zhao, M. Zheng, J. Yang, H. Qin, Z. Du, Z.L. Wang, Managing and maximizing the output power of a triboelectric nanogenerator by controlled tip–electrode air-discharging and application for UV sensing, Nano Energy 44 (2018) 208–216.
[7] J. Wang, X. Li, Y. Zi, S. Wang, Z. Li, L. Zheng, F. Yi, S. Li, Z.L. Wang, A flexible fiber-based supercapacitor–triboelectric-nanogenerator power system for wearable electronics, Adv. Mater. 27 (2015) 4830–4836.
[8] X. Cao, Y. Jie, N. Wang, Z.L. Wang, Triboelectric nanogenerators driven self-powered electrochemical processes for energy and environmental science, Adv. Energy Mater. 6 (2016) 1600665.
[9] D.P. Dubal, N.R. Chodankar, D.-H. Kim, P. Gomez-Romero, Towards flexible solid-state supercapacitors for smart and wearable electronics, Chem. Soc. Rev. 47 (2018) 2065–2129.
[10] S. Jiao, A. Zhou, M. Wu, H. Hu, Kirigami patterning of MXene/bacterial cellulose composite paper for all-solid-state stretchable micro-supercapacitor arrays, Adv. Sci. 6 (2019) 1900529.
[11] C. Zhang, Z. Peng, Y. Chen, H. Chen, B. Zhang, H. Cheng, J. Wang, M. Deng, Efficient coupling of semiconductors into metallic MnO_2@$CoMn_2O_4$ heterostructured electrode with boosted charge transfer for high-performance supercapacitors, Electrochim. Acta (2020) 136246.
[12] J. Lin, Z. Peng, Y. Liu, F. Ruiz-Zepeda, R. Ye, E.L. Samuel, M.J. Yacaman, B.I. Yakobson, J.M. Tour, Laser-induced porous graphene films from commercial polymers, Nat. Commun. 5 (2014) 1–8.
[13] N.A. Kyerematen, T. Brousse, D. Pech, Microsupercapacitors as miniaturized energy-storage components for on-chip electronics, Nat. Nanotechnol. 12 (2017) 7–15.
[14] M.R. Lukatskaya, S. Kota, Z. Lin, M.-Q. Zhao, N. Shpigel, M.D. Levi, J. Halim, P.-L. Taberna, M.W. Barsoum, P. Simon, Ultra-high-rate pseudocapacitive energy storage in two-dimensional transition metal carbides, Nat. Energy 2 (2017) 1–6.
[15] P. Zhang, F. Wang, M. Yu, X. Zhuang, X. Feng, Two-dimensional materials for miniaturized energy storage devices: from individual devices to smart integrated systems, Chem. Soc. Rev. 47 (2018) 7426–7451.

[16] J. Ju, J. Ma, Y. Wang, Y. Cui, P. Han, G. Cui, Solid-state energy storage devices based on two-dimensional nano-materials, Energy Stor. Mater. 20 (2019) 269–290.
[17] S. Bai, N. Zhang, C. Gao, Y. Xiong, Defect engineering in photocatalytic materials, Nano Energy 53 (2018) 296–336.
[18] Y. Lin, K. Sun, S. Liu, X. Chen, Y. Cheng, W.C. Cheong, Z. Chen, L. Zheng, J. Zhang, X. Li, Construction of CoP/NiCoP nanotadpoles heterojunction interface for wide pH hydrogen evolution electrocatalysis and supercapacitor, Adv. Energy Mater. 9 (2019) 1901213.
[19] D. Feng, T. Lei, M.R. Lukatskaya, J. Park, Z. Huang, M. Lee, L. Shaw, S. Chen, A.A. Yakovenko, A. Kulkarni, Robust and conductive two-dimensional metal-organic frameworks with exceptionally high volumetric and areal capacitance, Nat. Energy 3 (2018) 30–36.
[20] J.Y. Hwang, M.F. El-Kady, Y. Wang, L. Wang, Y. Shao, K. Marsh, J.M. Ko, R.B. Kaner, Direct preparation and processing of graphene/RuO_2 nanocomposite electrodes for high-performance capacitive energy storage, Nano Energy 18 (2015) 57–70.
[21] C. Zhang, Y. Huang, S. Tang, M. Deng, Y. Du, High-energy all-solid-state symmetric supercapacitor based on Ni_3S_2 mesoporous nanosheet-decorated three-dimensional reduced graphene oxide, ACS Energy Lett. 2 (2017) 759–768.
[22] C. Zhang, J. Wei, L. Chen, S. Tang, M. Deng, Y. Du, All-solid-state asymmetric supercapacitors based on Fe-doped mesoporous Co_3O_4 and three-dimensional reduced graphene oxide electrodes with high energy and power densities, Nanoscale 9 (2017) 15423–15433.
[23] M.Z. Iqbal, M.M. Faisal, S.R. Ali, M. Alzaid, A facile approach to investigate the charge storage mechanism of MOF/PANI based supercapattery devices, Solid State Ion. 354 (2020) 115411.
[24] M. Schumann, R. Sauerbrey, M. Smayling, Permanent increase of the electrical conductivity of polymers induced by ultraviolet laser radiation, Appl. Phys. Lett. 58 (1991) 428–430.
[25] A.C. Ferrari, J. Meyer, V. Scardaci, C. Casiraghi, M. Lazzeri, F. Mauri, S. Piscanec, D. Jiang, K. Novoselov, S. Roth, Raman spectrum of graphene and graphene layers, Phys. Rev. Lett. 97 (2006) 187401.
[26] B. Sun, R.N. McCay, S. Goswami, Y. Xu, C. Zhang, Y. Ling, J. Lin, Z. Yan, Gas-permeable, multifunctional on-skin electronics based on laser-induced porous graphene and sugar-templated elastomer sponges, Adv. Mater. (2018) 1804327.
[27] L. Yang, N. Yi, J. Zhu, Z. Cheng, X. Yin, X. Zhang, H. Zhu, H. Cheng, Novel gas sensing platform based on a stretchable laser-induced graphene pattern with self-heating capabilities, J. Mater. Chem. A 8 (2020) 6487–6500.
[28] W. Lu, Y. Li, M. Yang, X. Jiang, Y. Zhang, Y. Xing, Construction of hierarchical Mn_2O_3@ MnO_2 core-shell nanofibers for enhanced performance supercapacitor electrodes, ACS Appl. Energy Mater. 3 (2020) 8190–8197.
[29] C. Choi, D.S. Ashby, D.M. Butts, R.H. DeBlock, Q. Wei, J. Lau, B. Dunn, Achieving high energy density and high power density with pseudocapacitive materials, Nat. Rev. Mater. (2019) 1–15.
[30] M. Boota, Y. Gogotsi, MXene-conducting polymer asymmetric pseudocapacitors, Adv. Energy Mater. 9 (2019) 1802917.
[31] J. Chen, B. Yang, H. Hou, H. Li, L. Liu, L. Zhang, X. Yan, Potassium-ion batteries: disordered, large interlayer spacing, and oxygen-rich carbon nanosheets for potassium ion hybrid capacitor, Adv. Energy Mater. 9 (2019) 1970069.
[32] L. Yu, Z. Fan, Y. Shao, Z. Tian, J. Sun, Z. Liu, Versatile N-doped MXene ink for printed electrochemical energy storage application, Adv. Energy Mater. 9 (2019) 1901839.
[33] Z. Pei, H. Hu, G. Liang, C. Ye, Carbon-based flexible and all-solid-state micro-supercapacitors fabricated by inkjet printing with enhanced performance, Nanomicro Lett. 9 (2017) 19.
[34] X. Lang, A. Hirata, T. Fujita, M. Chen, Nanoporous metal/oxide hybrid electrodes for electrochemical supercapacitors, Nat. Nanotechnol. 6 (2011) 232–236.
[35] Y. Wang, S. Su, L. Cai, B. Qiu, N. Wang, J. Xiong, C. Yang, X. Tao, Y. Chai, Monolithic integration of all-in-one supercapacitor for 3D electronics, Adv. Energy Mater. 9 (2019) 1900037.
[36] J. Liang, H. Li, H. Li, X. Dong, X. Zheng, Y. Tao, Z. Weng, Z.H. Huang, Q.H. Yang, Building carbon-based versatile scaffolds on the electrode surface to boost capacitive performance for fiber pseudocapacitors, Small 15 (2019) 1900721.
[37] L. Zhang, H. Ji, H. Huang, N. Yi, X. Shi, S. Xie, Y. Li, Z. Ye, P. Feng, T. Lin, X. Liu, X. Leng, M. Li, J. Zhang, X. Ma, P. He, W. Zhao, H. Cheng, Wearable circuits sintered at room temperature directly on the skin surface for health monitoring, ACS Appl. Mater. Interfaces 12 (2020) 45504–45515.
[38] S. Xu, Y. Zhang, J. Cho, J. Lee, X. Huang, L. Jia, J.A. Fan, Y. Su, J. Su, H. Zhang, Stretchable batteries with self-similar serpentine interconnects and integrated wireless recharging systems, Nat. Commun. 4 (2013) 1–8.
[39] L. Li, Z. Lou, W. Han, D. Chen, K. Jiang, G. Shen, Highly stretchable micro-supercapacitor arrays with hybrid MWCNT/PANI electrodes, Adv. Mater. Technol. 2 (2017) 1600282.
[40] J. Yun, C. Song, H. Lee, H. Park, Y.R. Jeong, J.W. Kim, S.W. Jin, S.Y. Oh, L. Sun, G. Zi, Stretchable array of high-performance micro-supercapacitors charged with solar cells for wireless powering of an integrated strain sensor, Nano Energy 49 (2018) 644–654.
[41] Y. Wu, H. Hu, C. Yuan, J. Song, M. Wu, Electrons/ions dual transport channels design: concurrently tuning interlayer conductivity and space within re-stacked few-layered MXenes film electrodes for high-areal-capacitance stretchable micro-supercapacitor-arrays, Nano Energy (2020) 104812.
[42] D. Kim, G. Shin, Y.J. Kang, W. Kim, J.S. Ha, Fabrication of a stretchable solid-state micro-supercapacitor array, ACS Nano 7 (2013) 7975–7982.
[43] G. Lee, D. Kim, D. Kim, S. Oh, J. Yun, J. Kim, S.-S. Lee, J.S. Ha, Fabrication of a stretchable and patchable array of high performance micro-supercapacitors using a non-aqueous solvent based gel electrolyte, Energy Environ. Sci. 8 (2015) 1764–1774.
[44] D. Qi, Z. Liu, Y. Liu, W.R. Leow, B. Zhu, H. Yang, J. Yu, W. Wang, H. Wang, S. Yin, Suspended wavy graphene microribbons for highly stretchable microsupercapacitors, Adv. Mater. 27 (2015) 5559–5566.
[45] S.Y. Hong, J. Yoon, S.W. Jin, Y. Lim, S.-J. Lee, G. Zi, J.S. Ha, High-density, stretchable, all-solid-state microsupercapacitor arrays, ACS Nano 8 (2014) 8844–8855.
[46] H. Kim, J. Yoon, G. Lee, S.-H. Paik, G. Choi, D. Kim, B.-M. Kim, G. Zi, J.S. Ha, Encapsulated, high-performance, stretchable array of stacked planar micro-supercapacitors as waterproof wearable energy storage devices, ACS Appl. Mater. Interfaces 8 (2016) 16016–16025.
[47] H. Chen, L. Bai, T. Li, C. Zhao, J. Zhang, N. Zhang, G. Song, Q. Gan, Y. Xu, Wearable and robust triboelectric nanogenerator based on crumpled gold films, Nano Energy 46 (2018) 73–80.
[48] H. Chen, L. Lv, J. Zhang, S. Zhang, P. Xu, C. Li, Z. Zhang, Y. Li, Y. Xu, J. Wang, Enhanced stretchable and sensitive strain sensor via controlled strain distribution, Nanomaterials 10 (2020) 218.
[49] D. Kim, D. Kim, H. Lee, Y.R. Jeong, S.J. Lee, G. Yang, H. Kim, G. Lee, S. Jeon, G. Zi, Body-attachable and stretchable multisensors integrated with wirelessly rechargeable energy storage devices, Adv. Mater. 28 (2016) 748–756.
[50] N. Yi, Z. Cheng, H. Li, L. Yang, J. Zhu, X. Zheng, Y. Chen, Z. Liu, H. Zhu, H. Cheng, Stretchable, ultrasensitive, and low-temperature NO_2 sensors based on MoS_2@rGO nanocomposites, Mater, Today Phys. 15 (2020) 100265.

Biography

Cheng Zhang received a B.S. degree from the Department of Physics, Huanggang Normal University, China, in 2010. He received a Ph.D. degree from Nanjing University in 2018. He is now an assistant professor at Minjiang University, China. His research interests include the synthesis, fabrication, and assembly of inorganic materials for energy and environmental applications.

Zhixiang Peng received his BS degree from the Department of Materials Science and Engineering, Fujian Agriculture and Forestry University, China in 2019. He is currently a Research Assistant at Minjiang University. His research work interests focus on Crumpled graphene, Stretchable and Flexible sensors, Energy Harvesting Devices.

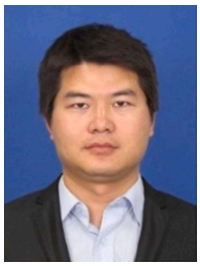

Chunlei Huang received her Ph.D. degree in Materials Science from Shanghai Institute of Optics and Fine Mechanics (SIOM), Chinese Academy of Science (CAS) in 2018. He is now an assistant professor at Minjiang University, China. His research interests are plasmonic nanostructures.

Bingwen Zhang received a Ph.D. degree from Nanjing University in 2019. He is currently an assistant professor at the Fujian Provincial Key Laboratory of Functional Marine Sensing Materials, Minjiang University, China. His research work is focused on piezoelectric sensors and spintronic devices

Chao Xing received his Ph.D. degree in 2015 from the College of Chemistry, Fuzhou University. He is an associate professor at Minjiang University. His research interests focus on DNA nanotechnology, including the development of DNA sensing and amplification schemes, DNA computing, and DNA machines.

Huamin Chen received his B. S. degree from Fudan University in 2014. He received his Ph. D degree from the Institute of Semiconductors, Chinese Academy of Sciences, in 2019. He is now an associate professor at Minjiang University. His research interest includes Crumpled graphene, Stretchable and Flexible electronics, Energy Harvesting Devices, and Microfabrication.

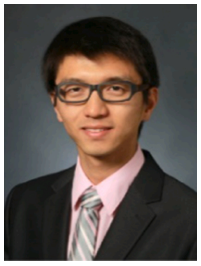

Prof. Huanyu Cheng earned a Ph.D. degree from Northwestern University in 2015 and a Bachelor's degree from Tsinghua University in 2010. After his doctoral study, he was appointed as the Dorothy Quiggle Assistant Professor of Engineering Science and Mechanics at Penn State University. Dr. Cheng has worked on the design, fabrication, and application of biologically inspired electronics for biomedicine. Dr. Cheng has co-authored over 90 publications, and his work has been recognized through the reception of numerous awards. He also serves as an associate editor for *Computers in Biology and Medicine* and reviewer for over 120 journals.

Jun Wang received Ph. D degree from the University of Science and Technology of China (USTC). He is now a professor at Minjiang University. His research interest includes the chemical and physical properties of the micro-nano structure, Magnetic Sensing Devices and Microfabrication, and assembly of inorganic materials for energy and environmental applications.

Shaolong Tang received his Ph.D. in physics from the Institute of Metal Research, Academia Sinica, Chinese Academy of Sciences in 1997. he has been a Professor of physics at Nanjing University. His research interests include magnetic materials synthesis, characterization, modifications, and applications in nano- and biosensors, clean energy, (opto-)electronic devices, catalysis, and water remediation, etc.